ACS OMEGA

Article

Cite This: ACS Omega 2018, 3, 8317−8328

Drug-Carrying Capacity and Anticancer Effect of the Folic Acid- and Berberine-Loaded Silver Nanomaterial To Regulate the AKT-ERK Pathway in Breast Cancer

Ramasamy Bhanumathi, Manickam Manivannan, Ramasundaram Thangaraj, and Soundarapandian Kannan*

Division of Cancer Nanomedicine, Department of Zoology, Periyar University, Salem 636 011, Tamil Nadu, India

Supporting Information

ABSTRACT: Currently, in clinics, breast cancer is treated with free chemotherapeutic drugs, as a result there is not much therapeutic effect in treated models, leading to substantial systemic toxicity. To overcome these critical problems for the primary outcome, we developed the formulated nanomaterial (FA-PEG@BBR-AgNPs) aimed to specifically target cancer cells via nanoscopic-based drug delivery for getting better therapeutic effectiveness. In the present study, an isoquinoline alkaloid, berberine (BBR), was chosen as a cancer therapeutic agent, encapsulated on citrate-capped silver nanoparticles (AgNPs) through electrostatic interactions (BBR-AgNPs). Then, BBR-AgNPs were conjugated with polyethylene glycol-functionalized folic acid (FA-PEG) via hydrogen bonding interactions (FA-PEG@BBR-AgNPs). The transmission electron microscopy study shows the cellular invasion of the formulated FA-PEG@BBR-AgNPs, indicating the accretion of the nanomaterial at the tumor-specific site. Hence, FA conjugated with the nanomaterial suggests an efficient release of BBR molecules into the specific cancer site. Consequently, the results showed an increase in apoptotic induction via reactive oxygen species and condensed nuclei in cancer cells. Moreover, the western blotting analysis shows reduced/increased expression of PI3K, AKT, Ras, Raf, ERK, VEGF, HIF1α, Bcl-2, Bax, cytochrome *c*, caspase-9, and caspase-3, thereby enhancing apoptosis. Likewise, the in vivo antitumor efficiency of FA-PEG@BBR-AgNPs showed a significant restraint of tumor progression, and histopathological observations of lung, liver, kidney, heart, and brain tissues proved lesser toxicity of FA-PEG@BBR-AgNPs. Thus, the successfully formulated nanomaterial can serve as a potential drug-discharging vehicle to combat cancer cells by a molecular-based targeting approach.

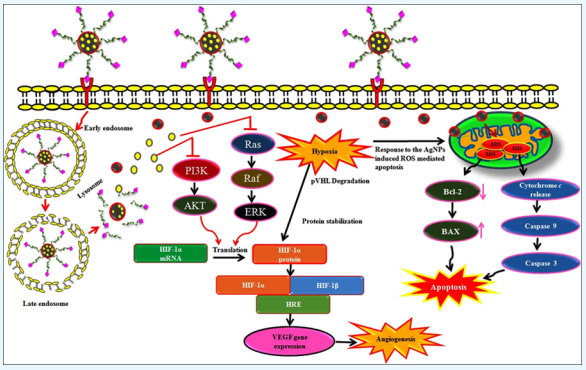

INTRODUCTION

Breast cancer is the most frequently diagnosed cancer among females worldwide and the second foremost cause of cancer death.[1] In 2017, the total estimate was stated as 252 710 cases of invasive breast cancer and 40 610 deaths in the United States.[2,3] Typically, the fast expansion, metastasis, and angiogenesis of breast tumors owing to the imbalance in the supply of cellular O_2 signify hypoxia.[4−6] The PI3K/AKT and Ras/Raf/MEK/ERK molecular signaling network commonly play a central role in the alteration of several human cancers because these pathways are involved in cellular physiological functions such as proliferation, survival, differentiation and metabolism, and cell mobility. Activation of these signaling pathways is accountable for unrestrained cell proliferation and activation of these drug resistance ability.[7,8] In addition, the PI3K/AKT and Ras/Raf/ERK signaling network is a primary regulator of hypoxia by activating the HIF-1α protein. The cancer cells with the hypoxic condition generate excessive levels of superoxides, peroxides, hydroxyl radicals, and singlet oxygens, collectively represented as reactive oxygen species (ROS) that promote angiogenesis, aggressive phenotypes, drug resistance, and metastasis in cancer cells.[9,10] Nowadays, the field of nanotechnology is generating new tools and techniques in biomedical fields for getting better treatment strategies to control or cure the disease at molecular levels. In this regard, the effective delivery of drug molecules combined with nanoparticles (NPs) improves the treatment strategies of cancer. Besides, the naturally occurring berberine (BBR) as an isoquinoline alkaloid causes cell cycle arrest, cell growth inhibition, and cellular apoptosis, suppresses cell migration and invasion in cancer cells through the intrinsic pathway,[11−14] as well as inhibits the phosphorylation of PI3K/AKT and Raf/MEK/ERK signaling pathways, consequently reducing the expression of hypoxia-induced proteins.[15] Free administration of BBR specifically in in vivo conditions causes low aqueous solubility, little gastrointestinal uptake, and rapid metabo-

Received: September 12, 2017
Accepted: November 28, 2017
Published: July 26, 2018

DOI: 10.1021/acsomega.7b01347
ACS Omega 2018, 3, 8317−8328

Scheme 1. Schematic Illustration Reveals the Loading of BBR on the Surface of Citrate-Capped AgNPs (BBR-AgNPs) Occurred through the Electrostatic Interactions and FA-PEG Conjugated with BBR-AgNPs (FA-PEG@BBR-AgNPs) through Hydrogen Bond Interaction

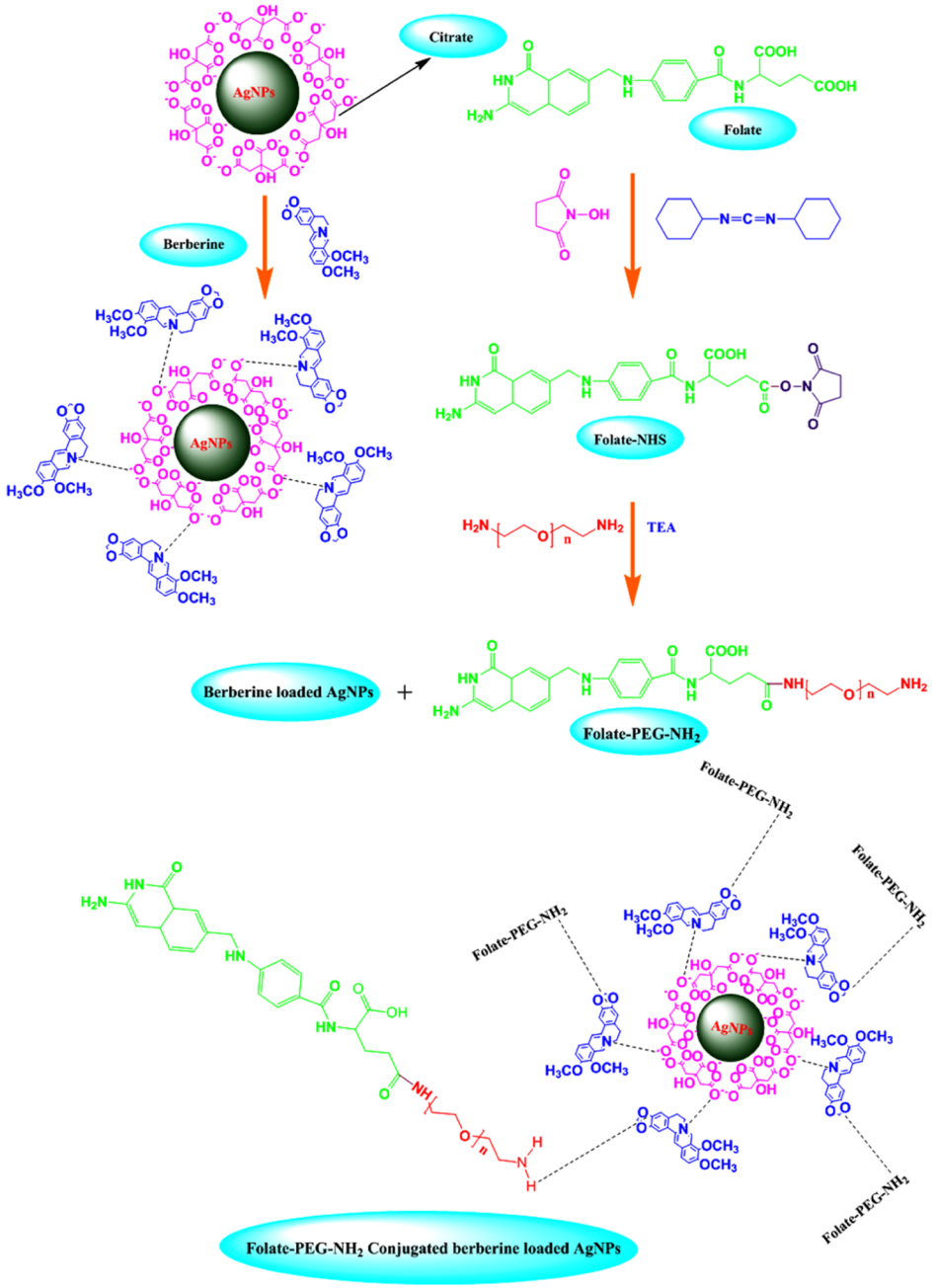

lism.[16,17] In this context to overcome these obstacles, NP formulations have been used to improve bioavailability and reduce water solubility efficiently. Of late, silver nanoparticles (AgNPs) are the most relevant NPs owing to their influence on significant genotoxic effects and programmed cell death (apoptosis) in cancer cells. Recently, Jeong et al. have reported that obstructing AgNPs induced ROS-mediated apoptotic pathways in cancerous cells.[18] Mostly, the therapeutic efficacy of a nanodrug system depends upon its targeting ability and stimulation of responsive cargo release into tissues/cells. Moreover, a tumor-targeted molecule, folic acid (FA), authorizes the cancer cell endocytosis and NP accumulation by recognizing its counterpart, which is over-expressed on many cancer cell surfaces.[19] Thus, labeling of folic acid functionalized with polyethylene glycol (PEG) on NPs could be a healthier method for specifically targeting cancer cells as well as providing high solubility, prolonged circulation time, and superior biocompatibility to the formulated nanomaterial.[20]

In the present study, citrate-capped AgNPs are fabricated and loaded with BBR through electrostatic interactions and conjugated with FA-PEG by hydrogen bonding interactions, denoted as the FA-PEG@BBR-AgNP drug delivery system that is used as a therapeutic agent for breast carcinoma. Our research mainly focuses on developing a new nanomaterial, which acts by using the combined effect of AgNPs and BBR via the folate receptor. Moreover, the effectively invasive FA-PEG@BBR-AgNP nanomaterial could be more promising in eliciting molecular-based novel therapeutic effect by targeting

DOI: 10.1021/acsomega.7b01347
ACS Omega 2018, 3, 8317−8328

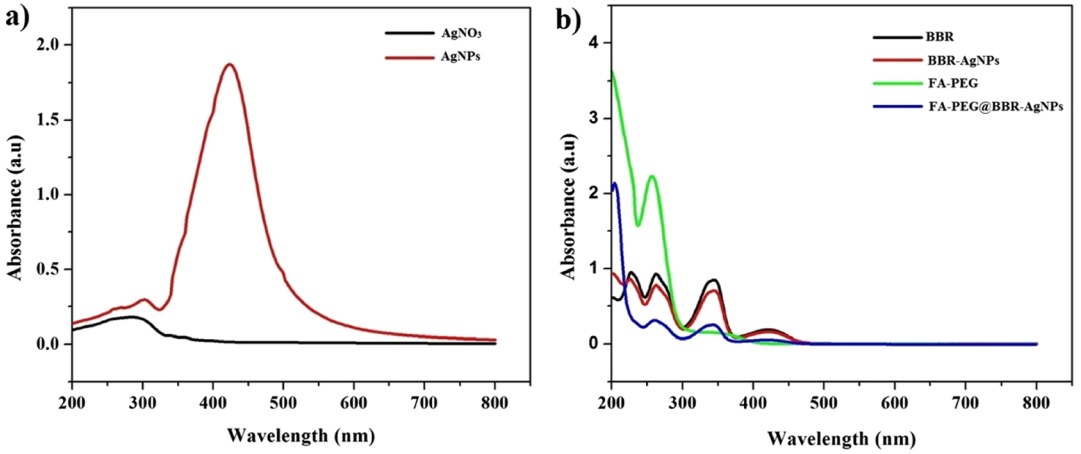

Figure 1. UV−visible spectrum: (a) $AgNO_3$ and AgNPs. (b) BBR, BBR-AgNPs, FA-PEG, and FA-PEG@BBR-AgNPs.

PI3K/AKT and Ras/Raf/ERK signaling pathways, thus reducing the hypoxia condition in breast cancer cells. Therefore, the formulated nanomaterials comprise BBR with AgNPs to target PI3K/AKT and Ras/Raf/ERK signaling pathways and induce severe ROS generations as well as the use of the PEG-altered drug delivery system demonstrates a very significant effect on breast cancer cells. Additionally, in vitro and in vivo studies were performed to investigate the antitumor effectiveness of the FA-PEG@BBR-AgNP nanomaterial.

RESULTS AND DISCUSSION

Synthesis and Characterization of FA-PEG@BBR-AgNPs. AgNPs acts as an efficient drug delivery agent as well as exhibits intrinsic anticancer activity.[25] The chemical method was followed by the synthesis of citrate-capped AgNPs; the trisodium citrate serves as a reducing agent for reducing silver salts. The negatively charged citrate anions assembled into the surface of the AgNPs. The BBR was positively charged cations, which readily bind with citrate anion-surfaced AgNPs through electrostatic interactions. Then, PEG-amine was chosen as the linker between FA and BBR-AgNPs using hydrogen bond interactions. The reaction mechanism for the synthesis of FA-PEG@BBR-AgNPs is outlined in Scheme 1.

UV−Vis Spectroscopy Studies. UV−visible absorption spectra of silver nitrate ($AgNO_3$), AgNPs, BBR-AgNPs, FA-PEG, and FA-PEG@BBR-AgNPs are presented in Figure 1. UV−vis spectra are usually the predictable method for studying the formation of NPs in aqueous suspension.[26] Figure 1a shows the UV−vis spectra of $AgNO_3$ and synthesized AgNPs, which reveals that new absorption peaks at 428 nm appeared only for AgNPs. Figure 1b shows the UV−vis spectra of BBR and BBR-AgNPs, FA-PEG, and FA-PEG@BBR-AgNPs. The major absorption peaks at 232, 266, 346, and 428 nm represented BBR; similar peaks were observed by Dai et al.[27] The successful loading of BBR on the surface of AgNPs was evident from the presence of BBR-AgNPs. After interactions of BBR with AgNPs, the peaks were slightly changed from 232, 266, 346, and 428 nm to 230, 264, 348, and 428 nm, respectively, which confirmed the successful loading of BBR on the surface of the AgNPs via electrostatic interactions. Subsequently, FA-PEG showed the major absorption peaks at 275 and 365 nm. Afterward, FA-PEG was conjugated with BBR-AgNPs through hydrogen bonding interactions to synthesize FA-PEG@BBR-AgNPs, which showed absorption peaks at 220, 270, 350 and 430 nm.

Fourier-Transform Infrared Spectroscopy (FT-IR) Analysis. FT-IR is a suitable technique for determining the interaction of BBR on the AgNPs, as well as the conjugation of FA-PEG with BBR-AgNPs. Figure 2 shows the FT-IR spectra of

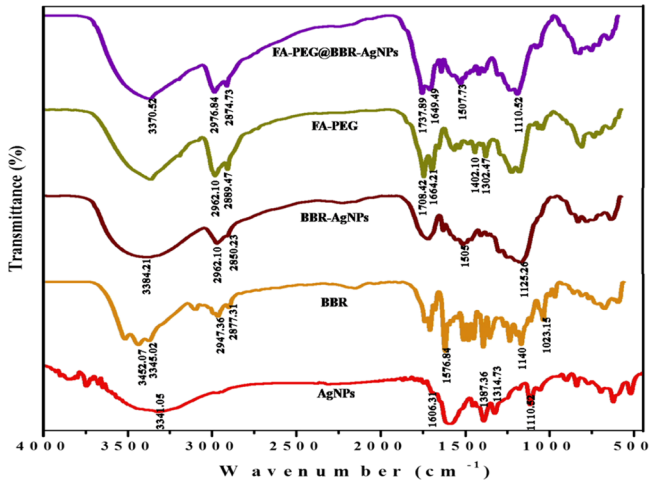

Figure 2. FT-IR spectra of AgNPs, BBR, BBR-AgNPs, FA-PEG, and FA-PEG@BBR-AgNPs.

AgNPs, BBR, BBR-AgNPs, FA-PEG, and FA-PEG@BBR-AgNPs. The significant bands of AgNPs at 3341 cm^{-1} are assigned to O−H stretching vibrations and the band at 1606 cm^{-1} corresponds to C═O stretching vibrations. The peaks at 1387, 1314, and 1110 cm^{-1} represent C−H stretching vibrations, and our results agree with those of Sharma and Tapadia.[28] The BBR exhibited significant bands at 3452 and 3345 cm^{-1} that represent N−H and O−H stretching vibrations, respectively. Other bands at 2947 and 2877 cm^{-1} correspond to C−H stretches (alkanes); likewise, peaks at 1576, 1140, and 1023 cm^{-1} correspond to aromatic C═C vibrations, CH in-plane bending, and C−H vibrations, respectively, and these major peaks are matched with the earlier report.[29] FT-IR was further extended to study about BBR-AgNPs, FA-PEG, and conjugated FA-PEG on the BBR-AgNPs (FA-PEG@BBR-AgNPs). The peak at 3384 cm^{-1}, corresponding to O−H stretching vibrations of BBR-AgNPs, shifted from the BBR peak at 3452 and 3345 cm^{-1}. The peaks at 1505 and 1125 cm^{-1} are

DOI: 10.1021/acsomega.7b01347
ACS Omega 2018, 3, 8317−8328

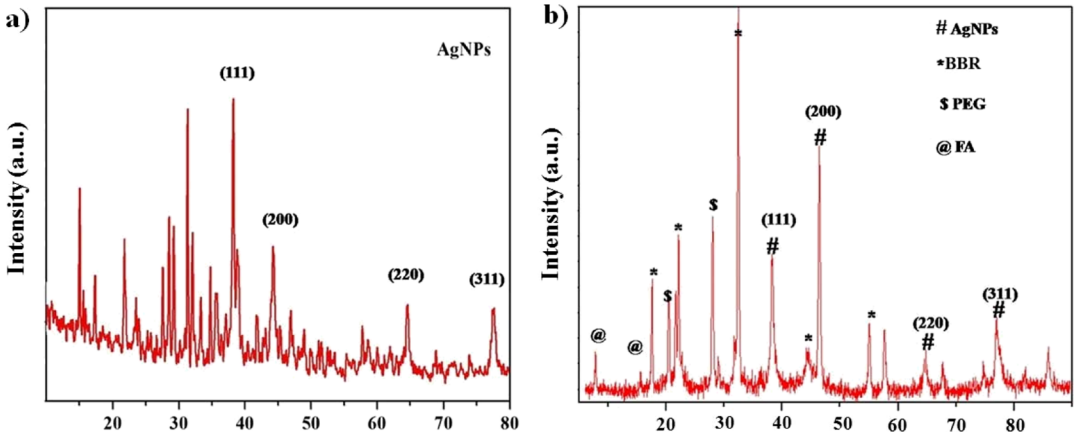

Figure 3. XRD analysis: (a) AgNPs and (b) FA-PEG@BBR-AgNPs.

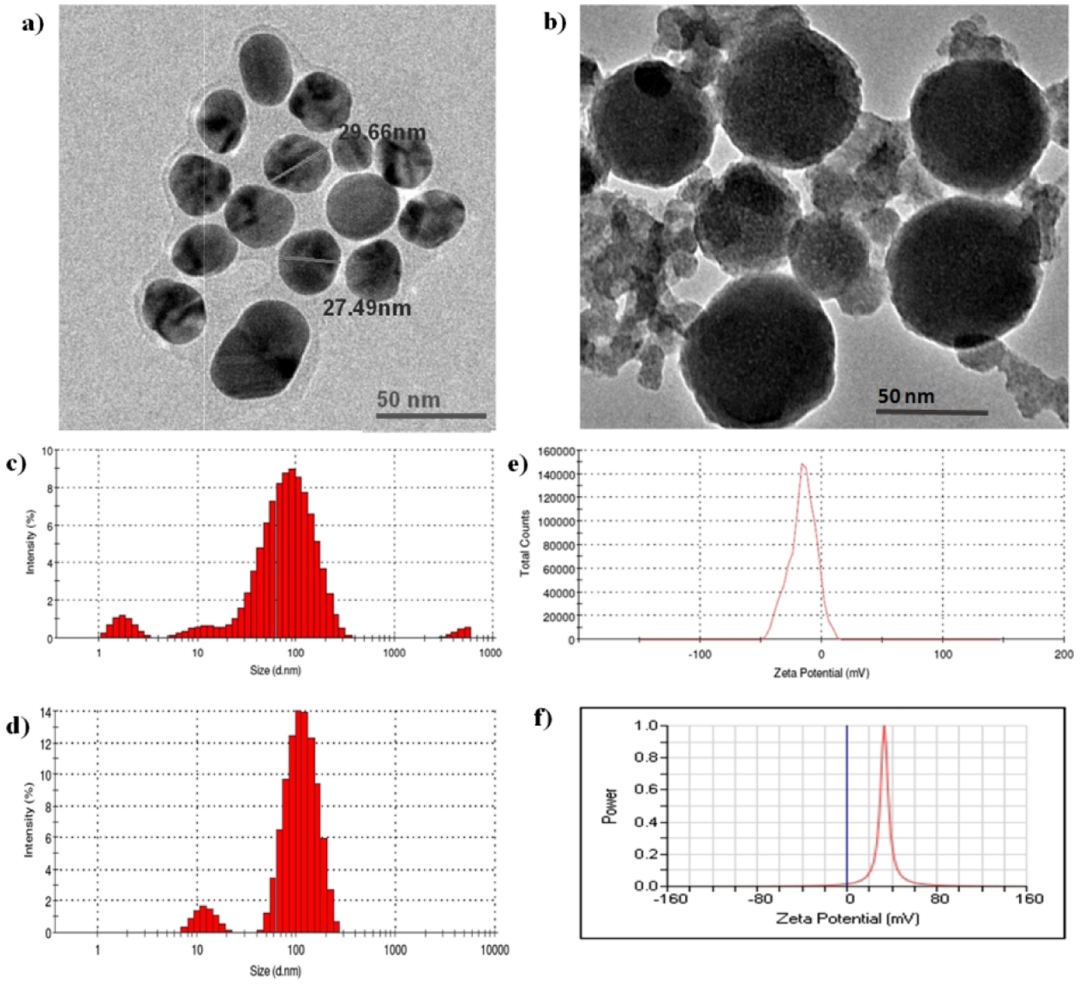

Figure 4. TEM micrograph: (a) AgNPs and (b) FA-PEG@BBR-AgNPs. Particle size distribution of AgNPs (c) and FA-PEG@BBR-AgNPs (d) with maximum intensity. Zeta potential of AgNPs (e) and (f) FA-PEG@BBR-AgNPs.

due to aromatic C═C vibrations, and the peak at 1140 cm^{-1} corresponding to C−H vibrations disappeared, which indicates no CH in-plane bending. The major characteristic peaks of the FA-PEG at 2962 and 2889 cm^{-1}, due to C−H stretches, correspond to asymmetric and symmetrical stretches, respectively. Bands at 1708, 1664, 1402, and 1302 cm^{-1} show C═O, C═C, C−C, and C−O stretch, respectively.[30] The FA-PEG@BBR-AgNPs were also confirmed through FT-IR spectroscopy; the peaks at 3370 cm^{-1} were due to the stretching vibrations of AgNPs. The BBR-AgNP bands at 2962 and 2850 cm^{-1}, representing C−H stretching (alkanes) and 1505 cm^{-1} (aromatic C═C vibrations) were shifted to 2976, 2874, and 1507 cm^{-1}. The other bands at 1708 and 1664 cm^{-1} are FA-PEG shifted to 1737 and 1649 cm^{-1}, which confirms the successful loading of FA-PEG on the surface of BBR-AgNPs.

DOI: 10.1021/acsomega.7b01347
ACS Omega 2018, 3, 8317−8328

X-Ray Diffraction (XRD) Analysis. The structural nature (crystal and phase purity) of the prepared AgNPs and FA-PEG@BBR-AgNPs was studied using the XRD patterns. The diffraction peaks at 38.11°, 44.01°, 65.01°, and 77.01° could be indexed to (111), (200), (220), and (311) planes of the face-centered cubic (fcc) crystal structure of AgNPs, respectively (Figure 3a), and well-matched with the Standard Joint Committee on Powder Diffraction data (JCPDS PDF no. 01-087-0717). Figure 3b shows the peaks at 17.11°, 24.02°, 45.12°, and 55.32°, indicating the peaks of BBR,[31] as well as peaks at 21.04° and 27.11° responsible for the presence of PEG moieties, and all other diffraction peaks observed at 8.02° and 16.33° were due to the presence of folic acid.[32]

Transmission Electron Microscopy (TEM), Dynamic Light Scattering (DLS), and Zeta Potential. The micrographs of AgNPs and FA-PEG@BBR-AgNPs are shown in Figure 4. Figure 4a shows that the monodispersed spherical-shaped AgNPs had an approximate size ranging from 20 to 30 nm. As illustrated in Figure 4b, the FA-PEG@BBR-AgNPs shows a slightly larger size with spherical shape approximately in the range of 50−60 nm. It is evident from Figure 4c,d that hydrodynamic diameters of the prepared NPs measured by DLS were 53 ± 2 nm (polydispersity index, PDI = 0.566 ± 0.07) for AgNPs and FA-PEG@BBR-AgNPs, and it was found to be 113 ± 4 nm (PDI = 0.297 ± 0.05). Furthermore, the electrostatic stabilization of NPs was estimated by measuring their zeta potential values (Figure 4e,f). The citrate-capped AgNPs are negatively charged (−15.6 mV), indicating that the surplus negative charge of AgNPs might be due to the capping with citrate.[33] The final product, FA-PEG@BBR-AgNP nanomaterial, possesses a positive charge (+33.28 mV).

Figure S1, illustrating the stability of the formulated FA-PEG@BBR-AgNPs in 10% mouse serum (mSerum) suspended in DMEM, reveals a slight change in size after 72 h. Subsequently, the obtained result exhibits that the formulated nanomaterial was found to remain stable under the physiological pH for 72 h (3 days). The positively charged nanomaterial improves the association and cellular internalization of negatively charged cell membranes.[34]

BBR Drug Loading Profile. To evaluate the encapsulation efficiency of BBR in the core−shell of AgNPs, the positively charged BBR encapsulated on the negatively charged AgNPs through electrostatic interactions. Loading efficacy of BBR-AgNPs was investigated by using a UV−vis spectrophotometer and theoretical DLC. Initially, free BBR appeared in dark yellow color; after being encapsulated into AgNPs, the color turned into brownish yellow, indicating the successful loading of BBR onto AgNPs. The BBR-loaded AgNPs exhibits the absorption peaks at 230, 264, 348, and 428 nm. The theoretical DLC was set at 10 wt %, and the results showed that the DLC of BBR-AgNPs was 8.79 wt %, and as a result, BBR was effectively loaded onto the citrate-capped AgNPs.

In Vitro Drug Release Study. The cumulative quantity of BBR liberated from the FA-PEG@BBR-AgNPs was (Figure 5) calculated under different pH conditions, for instance, 7.4 (corresponds to the circulatory system), 6.5 (pH of tumor tissue), and 5.5 (corresponds to the mature endosomes of tumor cells) at 37 °C, respectively. The drug release was found to be 7.3, 55.7, and 88.7% at pH 7.4, 6.5, and 5.5, respectively. An increased quantity of drug was released at pH 5.5 and 6.5 when compared to pH 7.4 (7.3%). The FA-PEG@BBR-AgNPs remains stable for a considerable period of circulation in the blood at pH 7.4 and thereby eliminates the premature burst release. The stability, to a large extent, can reduce the side effects of the drug on normal cells because the release of BBR from FA-PEG@BBR-AgNPs occurs by a pH-sensitive polymer PEG on the surface of the NPs and inhibits the release of BBR from the BBR-AgNPs at pH 7.4. On the contrary, the hydrolysis of PEG leads to simultaneous dissociation on the surface of the nanocarrier at low pH (pH 6.5 and 5.5). Consequently, it influences the discharge of BBR from PEG. Our obtained results suggested that the pH-responsive polymer-based BBR is released from FA-PEG@BBR-AgNPs in a controlled and sustainable manner.

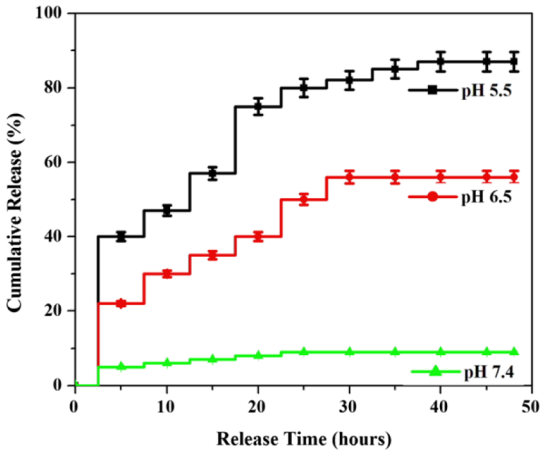

Figure 5. Cumulative BBR release (%) profile from FA-PEG@BBR-AgNPs at pH conditions 5.5, 6.5, and 7.4.

In Vitro Cytotoxicity Study. The cytotoxic effects of AgNPs, BBR, BBR-AgNPs, and FA-PEG@BBR-AgNPs were evaluated on MDA-MB-231 (breast cancer cell) and HBL-100 (normal breast cell) by the 3-(4,5-dimethylthialzol-2-yl)-2,5-diphenyltetrazolium bromide (MTT) assay. The treated HBL-100 cells by AgNPs, BBR, BBR-AgNPs, and FA-PEG@BBR-AgNPs at different concentrations of 1−14 μg/mL at 48 h. In the final concentration (14 μg/mL), inhibition rate was found to be 53% for AgNPs, 60% for BBR, 24% for BBR-AgNPs, and 18% for FA-PEG@BBR-AgNPs. A significant inhibition rate was observed with BBR and AgNPs when tested with HBL-100 cells (Figure 6a). The remaining BBR-AgNPs (24%) and FA-PEG@BBR-AgNPs (18%)-treated groups exhibit lesser toxic effect, indicating the biocompatibility of FA-PEG@BBR-AgNPs. However, the treatment of MDA-MB-231 by AgNPs, BBR, BBR-AgNPs, and FA-PEG@BBR-AgNPs at different drug concentrations (0.2−3 μg/mL) for 48 h showed an increased toxicity in a dose-dependent manner (Figure 6b). The IC_{50} concentration was found to be 1 μg/mL for FA-PEG@BBR-AgNPs. The FA-PEG@BBR-AgNPs exhibit significant inhibitory effects on MDA-MB-231 cells. The increased rate of inhibition effects on cell viability might be due to the targeted drug delivery system adopted via the folate receptor, which gets over-expressed in certain types of cancer cells.[19] On the other hand, there was a less toxic effect on normal cells (HBL-100).[35]

Analysis of Apoptotic Cells and Nuclear Morphology by Fluorescence Microscopy. The apoptosis induction was observed in the MDA-MB-231 cell line after treatment with FA-PEG@BBR-AgNPs at the IC_{50} concentration (1 μg/mL) for 48 h incubation. Briefly, the treated cells were stained with acridine orange/ethidium bromide (AO/EtBr) and observed using fluorescence microscopy. As can be seen in Figure 7a, untreated MDA-MB-231 cells (control) were stained with a

DOI: 10.1021/acsomega.7b01347
ACS Omega 2018, 3, 8317−8328

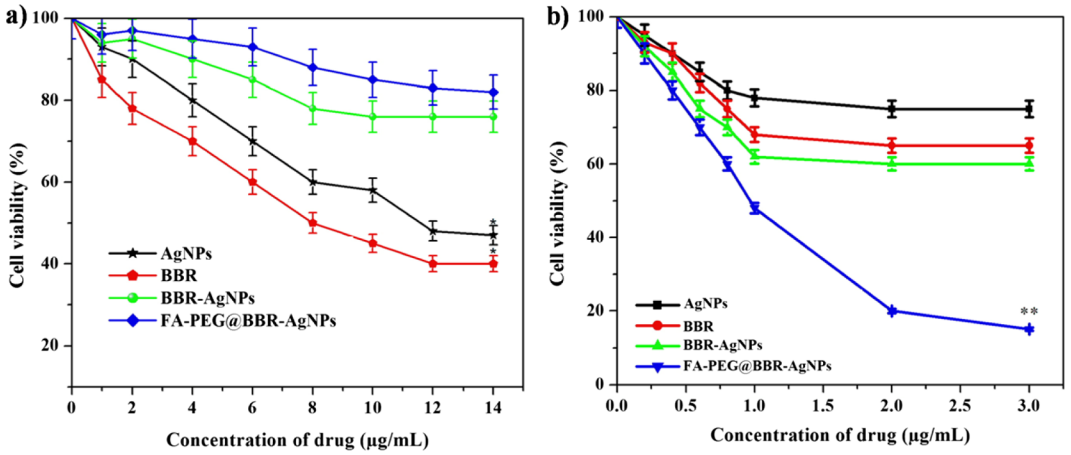

Figure 6. MTT assay results reveals the in vitro cytotoxicity effect of AgNPs, BBR, BBR-AgNPs, and FA-PEG@BBR-AgNPs against (a) normal breast cell lines (HBL-100) and (b) breast cancer cells MDA-MB-231 after incubation for 48 h, respectively. Data represent mean ± SD. $^{*}p \leq 0.05$ was considered statistically significant.

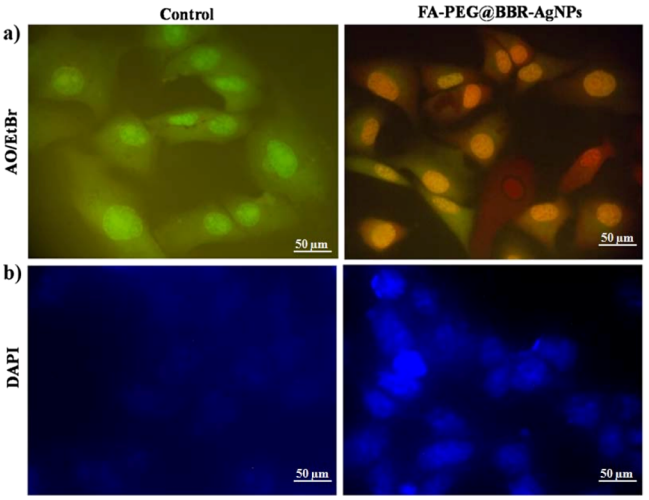

Figure 7. Fluorescent microscopic images of FA-PEG@BBR-AgNPs treated with MDA-MB-231 breast cancer cells. Cells were stained with AO/EtBr staining (a) shows the control and treated MDA-MB-231 cells. DAPI stain (b) for nuclear morphology in control and treated MDA-MB-231 cells.

similar green fluorescence image because the AO stain can only penetrate into the membrane of the normal cell. When compared with FA-PEG@BBR-AgNPs treated cells, orange color was observed because of their apoptotic condition. As a result, the cells exhibited nuclear shrinkage and bulging.[36,37]

DAPI (4′,6-diamidino-2-phenylindole) staining was used to study the nuclear morphology of the cells, as well as helps to differentiate the apoptotic nuclei from healthy cells. As can be seen from the images of Figure 7b, the untreated cells (control) exhibited a normal round nucleus morphology and discharged a weak fluorescence, whereas the FA-PEG@BBR-AgNPs nanomaterial-treated cells exhibited a significant nuclei fragmentation with the compression of apoptotic nuclei.

Intracellular ROS Generation. The intracellular oxidative stress induced via ROS generation was used to investigate the toxicological reports of nanomaterials.[38,39] The investigation about the capability of various materials such as AgNPs, BBR-AgNPs, and FA-PEG@BBR-AgNPs for intracellular ROS generation was analyzed by green fluorescence stain DCFH-DA. Under the normoxia condition, the AgNPs increased intracellular ROS generation in MDA-MB-231 cells (Figure 8a), compared to hypoxia pre-exposed DCF-positive cells. According to previous reports, under the hypoxia condition, AgNP treatment showed that the ROS generation reduced the percentage of DCF-positive cells.[18] Hence, in the present study, we used BBR-AgNPs and the FA-PEG@BBR-AgNPs for ROS generation, which was further enhanced in MDA-MB-231 cells under the hypoxia condition. From these results (Figure 8b), ROS scavenger DCFH-DA-stained BBR-AgNPs and FA-PEG@BBR-AgNPs treated MDA-MB-231 cells showed increased ROS generation under normoxia and hypoxia conditions.

Cellular Internalization of BBR-AgNPs and FA-PEG@BBR-AgNPs by TEM Analysis. TEM analysis was used to study the intracellular diffusion of the nanomaterial and the ultrastructural features of MDA-MB-231 breast cancer cells treated with BBR-AgNPs and FA-PEG@BBR-AgNPs. Figure 9 shows a significant cellular uptake through endocytosis and easy detachment of the polymeric background at intracellular acidic pH. This could elucidate the possible interaction of the nanomaterial with endolysosome membranes because of transitory undermining of the cell membranes, resulting in the easy entry of the nanomaterial into the cytosol.[40,41] At this stage, the BBR is released from FA-PEG@BBR-AgNPs, after the accretion of the nanomaterial in MDA-MB-231 cells. The aim of the study is to assess the MDA-MB-231 cell-targeting capability of the nanocarrier such as BBR-AgNPs and FA-PEG@BBR-AgNPs through FA receptor-binding efficacy (over-expressed in many types of cancer).[42]

In Figure 9a,b, the TEM images of BBR-AgNPs and FA-PEG@BBR-AgNPs treated MDA-MB-231 cells indicated the effectiveness of cellular internalization through different time intervals at 4, 12, and 24 h, respectively. This reveals a significant amount of cellular uptake of FA-PEG@BBR-AgNPs through the folate receptor, compared with BBR-AgNPs. Besides, the TEM images showed well-accretion of FA-PEG@BBR-AgNPs (red arrow) in the cytoplasm of the nucleus and mitochondria in MDA-MB-231 cells. On the other hand, the yellow arrows indicate the nuclear membrane fragmentation, as well as mitochondrial destruction, by the formulated FA-PEG@BBR-AgNPs in treated breast cancer cells. The above results show a significant amount of formulated nanomaterial accretion specifically high at tumor sites. The constructed nanoscopic-based targeted delivery system possesses necessary

DOI: 10.1021/acsomega.7b01347
ACS Omega 2018, 3, 8317−8328

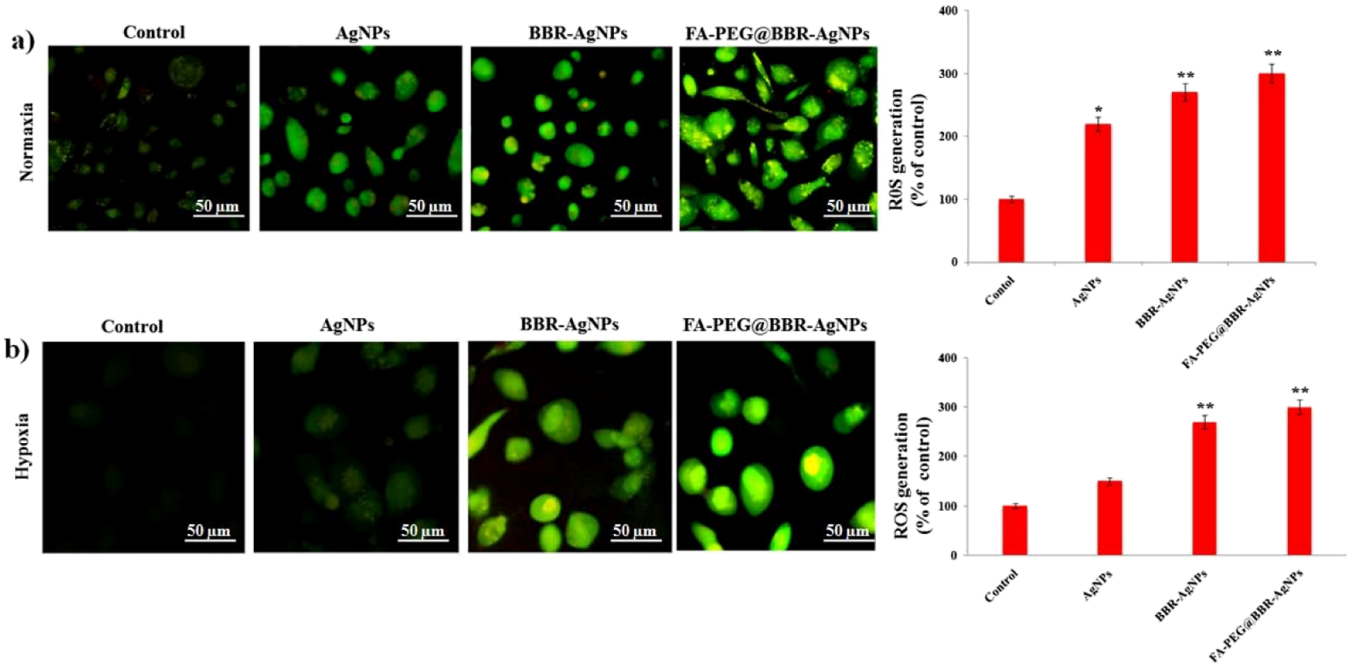

Figure 8. Fluorescence images: AgNPs, BBR-AgNPs, and FA-PEG@BBR-AgNPs mediated oxidative stress under normoxia (a) and hypoxia (b) condition using DCFH-DA as an ROS reactive fluorescent probe. The data represent mean ± SD $*p \leq 0.05$ was considered statistically significant.

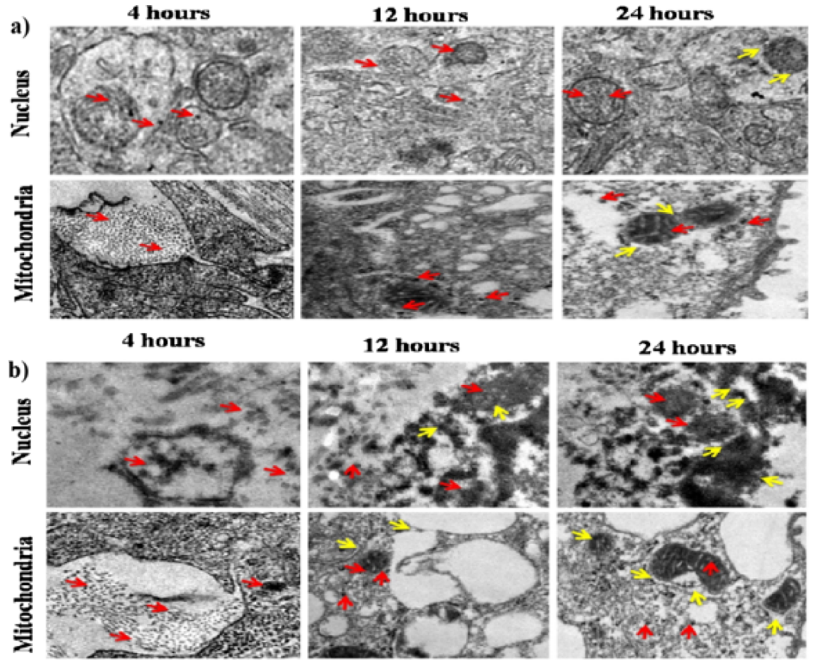

Figure 9. TEM images of cell organelles such as the nucleus and mitochondria of MDA-MB-231 breast cancer cells, sections after 4, 12, and 24 h of incubation with (a) BBR-AgNPs and (b) FA-PEG@BBR-AgNPs.

features, such as targeting a particular site, cell-type specificity, improved cellular uptake, and delivery to an acidic environment.[43] The internalization of nanomaterials have shown to possess significant therapeutic properties in FA over-expressed breast cancer cells.

Western Blot Analysis. The molecular-based activation of apoptosis in MDA-MB-231 breast cancer cells treated with FA-PEG@BBR-AgNPs was studied by western blot analysis. The expression levels of tumor progression proteins (PI3K, AKT, Ras, Raf, and ERK), angiogenesis protein (VEGF), hypoxia protein (HIF-1α), and mitochondrial-mediated apoptotic proteins (Bax, cytochrome *c*, caspase-9 and caspase-3) and antiapoptotic proteins (Bcl-2) were evaluated. The results show that the formulated FA-PEG@BBR-AgNPs treated cells caused the downregulation of tumor progression proteins such as PI3K, AKT, Ras, Raf, ERK, VEGF, and HIF-1α proteins (Figure 10a). The apoptotic regulator proteins were upregulated (Bax, cytochrome *c*, caspase-9, and caspase-3), whereas, the antiapoptotic protein (Bcl-2) was downregulated (Figure 10b). In our study, the adequately formulated FA-PEG@BBR-AgNPs in higher levels inhibits the expression of PI3K, AKT and Ras, Raf, and ERK, consequently blocking the binding of

DOI: 10.1021/acsomega.7b01347
ACS Omega 2018, 3, 8317−8328

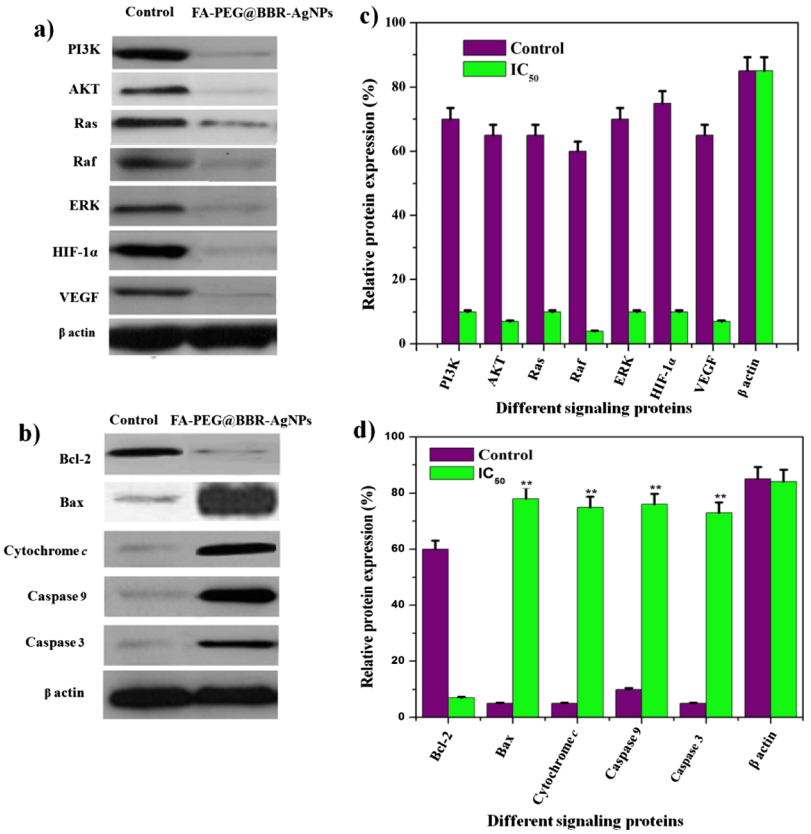

Figure 10. Western blot analysis showing expression of cellular response proteins (PI3K, AKT, Ras, Raf, and ERK), angiogenesis protein (VEGF), hypoxia protein (HIF-1α), apoptotic proteins (Bax, cytochrome *c*, caspase-9, and caspase-3), and antiapoptotic protein (Bcl-2) by MDA-MB-231 cells treated with FA-PEG@BBR-AgNPs (a–d).

the HIF-1α protein with HIF-1β. On the other hand, the AgNPs stimulate the depolarization of the mitochondrial membrane potential (MTP) and result in mitochondrial-attributed apoptosis via ROS production under the hypoxic condition, leading to the activation of the pro-apoptotic factors such as cytochrome *c*, caspase-9, and caspase-3 for the apoptosis to take place in breast cancer cells. The obtained results demonstrated that the downregulation of PI3K, AKT and Ras, Raf, ERK, VEGF, and HIF-1α triggered the apoptotic pathways (Figure 10a–d). Thus, the FA-PEG@BBR-AgNPs act as a valuable nanomaterial to activate the molecular-based stimulation of apoptosis in hypoxia-conditioned breast cancer cells.

In Vivo Antitumor Activity. The in vivo antitumor efficacy of AgNPs, BBR, BBR-AgNPs, and FA-PEG@BBR-AgNPs with a usage dose of 5 mg/kg body weight delivered intravenously into MDA-MB-231 tumor-bearing athymic nude mice was assessed. Followed by, recording the treatment strategy of various nanomaterials on tumor volume of mice group was evaluated after 24 days. The mice were treated with saline as a control group, and the tumor volume was increased quickly at 1287.27 ± 0.12 mm^3, indicating no significant tumor suppression. Subsequently, AgNPs (601 mm^3) and BBR (470 mm^3) show a moderate level of tumor growth suppression when compared to the control group. The BBR-AgNP-treated group had a tumor volume of 270 mm^3, and FA-PEG@BBR-AgNPs treated group had a volume of 101 mm^3 (Figure 11a). However, the obtained results indicate the significant tumor suppression observed in FA-PEG@BBR-AgNPs than others, owing to the fact that FA conjugation on the nanomaterial improves the cellular internalization as well as increases the drug discharging into cancer cells. Then, the body weight loss was evaluated, which showed variations in the animal body weight, helpful in in vivo toxicity study. Figure 11b demonstrates a gradual increase in the body weight of mice that are administered with saline. The decrease in the AgNP- and BBR-administered animal body weight when compared to other treated groups reveals that AgNPs and BBR can induce unfavorable effects at the specified dose concentration. However, BBR-AgNPs and FA-PEG@BBR-AgNPs administered mice group did not show any decrease in the body weight. Therefore, this result indicates that the formulated FA-PEG@BBR-AgNPs nanomaterial was nontoxic. Furthermore, the assessment of hematoxylin and eosin (H&E) staining for histological studies in treated mice groups (saline, AgNPs, BBR, BBR-AgNPs, and FA-PEG@BBR-AgNPs) indicates no significant damage to vital organs such as lungs, liver, kidneys, heart, and brain (Figure 11c). Although, the histological image of AgNPs and BBR-treated mice group shows acute inflammation, as well as organ injury in liver, heart, and kidneys, indicating that the free drug molecules can cause severe side effects in treated mice. Hence, using FA-PEG formulations with BBR-AgNPs, desired applications including biocompatibility, organ specificity, biodegradability, and targeted drug delivery can be obtained. Besides, at pH 7.4 corresponding to blood circulation, at this environment unfavorable for release of drugs, owing to stimulating the normal cell killing efficacy, but FA-PEG@BBR-AgNPs nanomaterial enhances the selective delivery of the drugs at tumor-specific sites (pH 5.5) by FA conjugation. Thus,

DOI: 10.1021/acsomega.7b01347
ACS Omega 2018, 3, 8317–8328

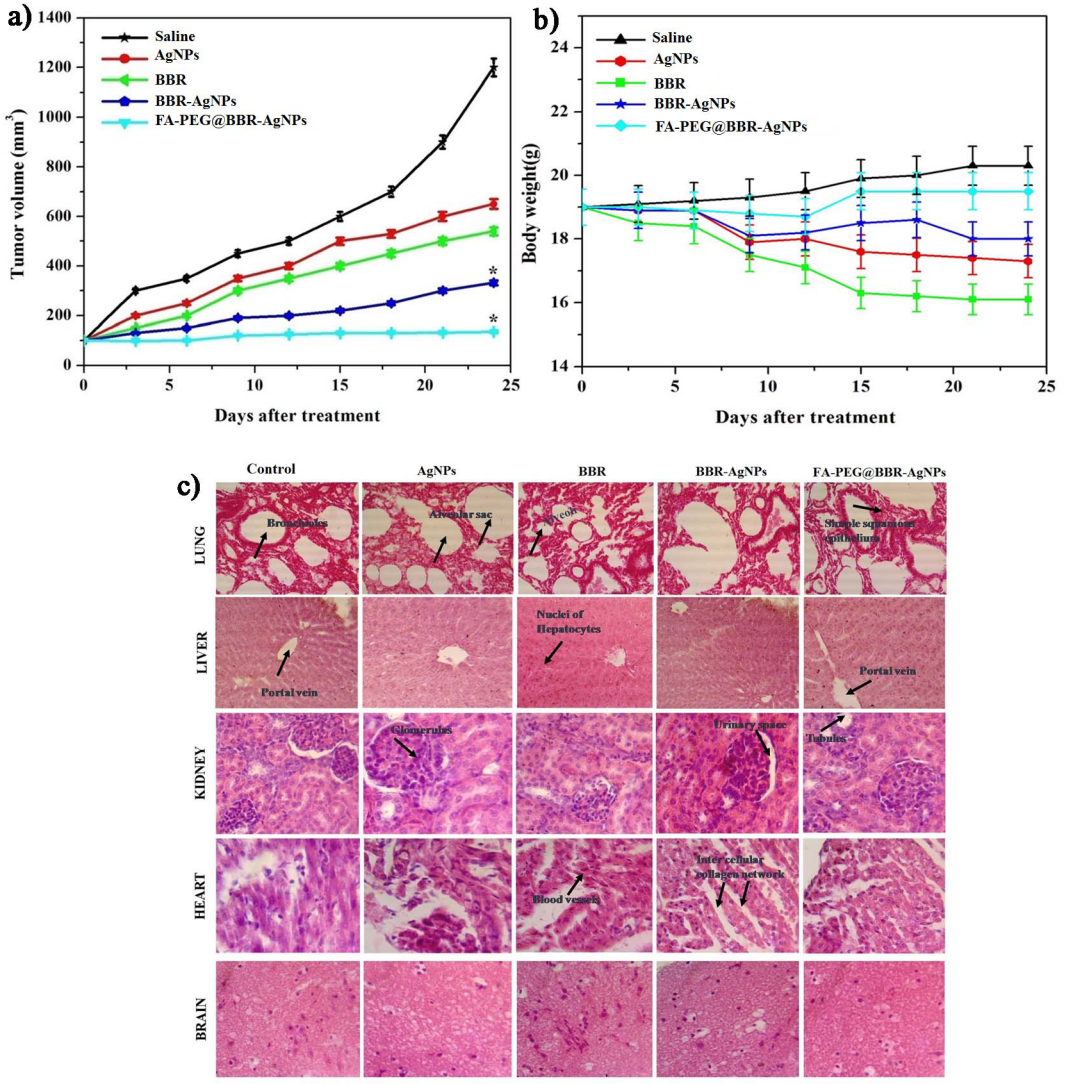

Figure 11. In vivo antitumor therapy. (a) Change in the tumor volume and (b) body weight of mice in five different treatment groups. Error bars are based on standard error of the mean. *$p \leq 0.05$ was considered statistically significant; (c) histopathological studies on lungs, liver, kidneys, heart, and brain in different treatments.

the formulated nanomaterial minimizes the side effects of drugs and increases the anticancer activity of breast cancer cells.

CONCLUSIONS

In summary, the prepared biocompatible FA-PEG@BBR-AgNPs based drug delivery specifically targeted the breast cancer cells. The formulated nanomaterial stimulates their cellular uptake by breast cancer cells, which was visualized by Bio-TEM images. The internalized nanomaterial disassembled their components including BBR & AgNPs into the cytoplasms of breast cancer cells, which synergistically induce cytotoxicity via the inhibition of PI3K/AKT and Ras/Raf/ERK protein expression to block the HIF-1α expression. Besides, the induction of depolarization in MTP to generate the highest level of ROS generation in mitochondria subsequently, to release the cytochrome *c*, and to activate the apoptotic pathway. Then, we verified the superior biocompatibility and tumor inhibition of the FA-PEG@BBR-AgNPs nanomaterial, and this reveals the effective inhibition of the tumor progression with no acute toxicity in vital organs. In this view, the formulated FA-PEG@BBR-AgNPs accomplished by precisely targeting the hypoxia condition via the downregulation of PI3K/AKT and Ras/Raf/ERK signaling networks, as a result of discrete therapeutic effectiveness and achieving severe synergistic cancer therapy with diminished tumor cell masses in mice models. Conclusively, the present finding shows the functionally upgraded FA-PEG@BBR-AgNPs as a prominent drug carrier, which could perform as an effective drug delivery for the molecular-based cancer therapy. Thus, the formulated nanomaterial (FA-PEG@BBR-AgNPs) might be a promising approach for targeted drug delivery in breast carcinoma.

MATERIALS AND METHODS

Materials. Silver nitrate ($AgNO_3$), trisodium citrate ($C_6H_5O_7Na_3{\cdot}2H_2O$), berberine hydrochloride, dimethyl sulfoxide (DMSO), PEG (MW 4000), folic acid (MW 441.4), *N*,*N*′-dicyclohexyl carbodiimide (DCC), and *N*-hydroxysuccinimide (NHS) were obtained from HiMedia. MTT, DAPI, and AO/EtBr were purchased from Sigma-Aldrich (India).

Synthesis of BBR-AgNPs and Drug Loading Content. In a typical procedure, the synthesis of AgNPs was followed by the previously reported method.[21] Then, 50 mg of AgNPs was

DOI: 10.1021/acsomega.7b01347
ACS Omega 2018, 3, 8317−8328

mixed with 50 mg of BBR in 10 mL of DMSO solution and stirred overnight. The reaction mixture was transferred to the dialyzer method at 25 °C for 24 h, respectively. After that, BBR-AgNPs were purified using a dialysis tube against ultrapure water to easily remove the unloaded BBR and DMSO solution.

The BBR loading efficacy of citrate-capped AgNPs was calculated by two methods: first, an indirect method by estimating the BBR content of the supernatant of the solution and, second, a direct method is the estimation of the BBR content present in the pellet obtained after centrifugation at 10 000 rpm for 30 min. The drug concentration in the supernatant and pellets was measured in UV absorbance at 345 nm by using UV−visible spectroscopy, and the percentage of loading BBR-AgNPs were estimated by the following formula.

$$\text{Loading efficiency} = \frac{w_o}{w} \times 100$$

where w_o is the weight of BBR loaded on the AgNPs and w is the weight of AgNPs.

Synthesis of Folic Acid-Polyethylene Glycol (FA-PEG). FA-PEG was prepared by a previously reported method with slight modification.[22] Briefly, about 10 mg of FA was reacted with DCC/NHS at a different ratio 10:5:5 in dimethyl sulfoxide (2.5 mL), which was stirred and kept in the dark for 5 h at 50 °C. Afterward, the reaction solution was mixed with 1 mg of PEG-bisamine (MW 4000) dissolved in a mixture of DMSO (2.5 mL) and then added with 0.1 mL of triethylamine. The mixture solution was stirred overnight at room temperature. The obtained product was isolated and purified by the dialysis method for the removal of unconjugated FA and unreacted PEG-bisamine.

Synthesis of FA-PEG@BBR-AgNP Nanomaterial. For the synthesis of the FA-PEG@BBR-AgNP nanomaterial, 20 mg of BBR-AgNPs in 10 mL phosphate-buffered saline (PBS, pH 7.4) was added using 0.5 mL FA-PEG amine and stirred for 24 h in 27 °C. Later, the final product was centrifuged and washed several times using Milli-Q water to remove unconjugated FA-PEG and dried overnight in a vacuum at 45 °C and used for further study.

Characterization of FA-PEG@BBR-AgNPs. The formation and stability of NPs in aqueous solution was determined using a UV−visible spectrophotometer (UV-1800, Shimadzu). The assessment of composition in NPs was carried out on a JASCO (FT-IR-400) spectrophotometer in the range of 400−4000 cm^{-1} using the KBr pellet technique. The nature of the NPs was analyzed by XRD, completely indexed to the fcc and well-matched with the available Joint Committee on Powder Diffraction Standards Ag (JCPDS PDF no. 01-087-0717). The morphology of AgNPs and FA-PEG@BBR-AgNPs was investigated using a TEM (EM TECNAI microscope). The particle surface charge (zeta potential) was measured by Nanotrac wave, and the average size distribution of NPs was determined by DLS using Mastersizer 3000. The stability of the formulated FA-PEG@BBR-AgNPs in 10% mouse serum in DMEM or 0.01 M phosphate buffer solution (pH 7.4) at 37 °C for 72 h was evaluated by dynamic light scattering (DLS).

BBR Release Assay. In vitro, the BBR release response from FA-PEG@BBR-AgNPs was carried out in systemic physiological pH of 7.4, 6.5, and 5.5 at 37 °C, respectively. The BBR discharge profiles from FA-PEG@BBR-AgNPs were measured by dialysis bag methods. Therefore, the FA-PEG@BBR-AgNPs (200 mg) was suspended in 1 mL PBS solution, permitted to stabilize the solution for 30 min, and positioned in a dialysis bag. The dialysis bag was submerged in 10 mL of PBS buffer solution having pH of 7.4, 6.5, and 5.5 and then incubated in a water bath at 37 °C and stirred at 110 rpm, respectively. At prearranged time intervals, 1 mL of PBS was collected from the medium to measure the released BBR quantity and replaced with the same new PBS solution. The BBR releasing concentration was measured at 420 nm to find out the level of BBR release from FA-PEG@BBR-AgNPs. All experiments were conducted in triplicate at each pH selected for the investigation.

Biological Experiment. *Cell Line and Culture Conditions.* For the cytotoxicity study of AgNPs, BBR, BBR-AgNPs, and FA-PEG@BBR-AgNPs on MDA-MB-231 (breast cancer cell) and HBL-100 (normal breast cell) were purchased from NCCS (National Centre for Cell Science) Pune, India. These cells were grown in 90% DMEM (Dulbecco's modified Eagles medium) and added with nonessential amino acids (0.1 mM), L-glutamine (2 mM), and fetal bovine serum (FBS, 10%) at 37 °C and 5% CO_2 condition.

In Vitro Cytotoxicity Studies. MTT assay was used to evaluate the cytotoxicity of AgNPs, BBR, BBR-AgNPs, and FA-PEG@BBR-AgNPs at different concentrations against HBL-100 normal breast cells and MDA-MB-231 breast cancer cells. Briefly, the breast cancer cells and normal breast cells were seeded into a 96-well plate at a density of 2×10^5 cells/well in 100 μL of complete Dulbecco's modified Eagles medium (DMEM) containing 10% FBS and nonessential amino acids and cultured for 1 day at 37 °C in a 5% CO_2 incubator. Subsequently, the breast cancer cells (0.2−3 μg/mL) and normal breast cells (1−14 μg/mL) were treated with various concentrations of AgNPs, BBR, BBR-AgNPs, and FA-PEG@BBR-AgNPs for 48 h. After incubation, MTT stock solution (5 mg/mL in PBS, 20 μL) was added to each well and incubated for another 4 h. The culture media were completely removed and added with 150 μL of dimethyl sulfoxide (DMSO) to each well to dissolve the formazan blue crystal. The absorbance was recorded using a microplate reader (Bio-TekELx800) at the wavelength of 572 nm.

Fluorescence Microscopic Studies. *AO/EtBr and DAPI Staining.* The cells were grown in a 6-well plate (2×10^6 cells/well) and treated with FA-PEG@BBR-AgNPs for 48 h. Then, the treated MDA-MB-231 cells were stained with 50 μL acridine orange (AO, 1 mg/mL) and ethidium bromide (EtBr, 1 mg/mL), and on the other hand, the MDA-MB-231 cells were stained with DAPI (nuclear staining). Later, the stained cells were washed with PBS and incubated for 20 min.[23] These cells were examined under a fluorescence microscope (Nikon Eclipse, Inc., Japan).

Determination of Intracellular ROS Levels. The determination of ROS production in MDA-MB-231 breast cancer cells were treated with AgNPs, BBR-AgNPs and PEG-FA@BBR-AgNPs (2 μg/mL) using the DCFH-DA stain was according to the method of Chen et al.[24] Briefly, the intracellular ROS production monitored in the cells (5×10^5 cells/well) was pipetted to a six-well plate and treated with various compounds (AgNPs, BBR-AgNPs and PEG-FA@BBR-AgNPs) for 24 h and stained with DCFH-DA (5 μg/mL). The ROS generation was observed through a fluorescence microscope (Nikon Eclipse, Inc., Japan) at 488 and 530 nm, respectively. Finally, the mean fluorescence intensity of DCF was evaluated by using a fluorescence plate reader.

TEM Analysis for Internalization of BBR-AgNPs and FA-PEG@BBR-AgNPs. The cellular internalization of BBR-AgNPs

DOI: 10.1021/acsomega.7b01347
ACS Omega 2018, 3, 8317−8328

and FA-PEG@BBR-AgNPs by MDA-MB-231 cells was evaluated. Briefly, the MDA-MB-231 cells were treated with BBR-AgNPs and FA-PEG@BBR-AgNPs, and then, the cells were washed with PBS buffer solution to remove the boundless BBR-AgNPs and FA-PEG@BBR-AgNPs. Then, the cells were fixed in glutaraldehyde (2.5%) for 30 min at 4 °C and washed with PBS buffer solution. Following, the different ratios of acetone and Spurr low viscosity resin was used in 3:1, 1:1, and 1:3 and incubated with beam capsules at 70 °C for 80 h, respectively. Microtome was used for 60 nm thickness cell section and then stained with 0.5% uranyl acetate and observed under a TEM microscope.

Western Blot Analysis. The MDA-MB-231 cells were treated with FA-PEG@BBR-AgNPs (1 μg/mL) and incubated for 24 h and then washed with ice-cold PBS buffer solution twice. Afterward, the cell extract was centrifuged for 5 min at 25 000 rpm to dispose the supernatant immediately. The centrifuged cells were washed with PBS solution and immersed in the lysis buffer containing (100 μL) Tris-HCl (50 mM), NaCl (150 mM), Triton X-100 (1%), phenylmethane-sulfonyl fluoride (1 mM), pepstatin (10 μg/mL), and leupeptin (10 μg/mL) at pH 8.0. The lysis buffer with cells was centrifuged for 10 min at 12 000 rpm at 4 °C, and the supernatants were stored at −80 °C for further use. The following 30 μg/lane proteins were separated using sodium dodecyl sulfate polyacrylamide gel electrophoresis (10%) and then transferred to polyvinylidene fluoride (PVDF) membranes. The PVDF membranes were blocked in Tris-buffered saline and Tween 20 (TBST) solution containing a nonfat milk (5% (w/v)) for 2 h, at 4 °C in overnight incubation with primary antibodies such as PI3K, AKT, Ras, Raf, ERK, HIF-1α, VEGF, Bax, Bcl-2, cytochrome *c*, caspase-9, caspase-3, and β-actin as a loading control in blots. The blots were washed with TBST buffer solution and tagged with secondary antibodies and combined with horseradish peroxidase for 1 h at ambient temperature.

In Vivo Anticancer Efficacy. As per the Institutional Animal Ethical Committee (IAEC) of Periyar University (PU/IAEC 1085/PO/OC/07/CPCSEA/ZOOC/04/2016), the in vivo study has been permitted and approved. Initially, the female athymic nude mice (5−6 week old) were subcutaneously injected with MDA-MB-231 cells (5×10^6). After 7 days, the mice were randomly divided into five groups with five mice in each group. The mice of group A, normal saline; group B, AgNPs; group C, BBR; group D, BBR-AgNPs; and group E; FA-PEG@BBR-AgNPs and the concentration of 5 mg/kg body weight were injected intravenously via tail every 2 days for 24 days. After the experimental period, the tumor volume of mice was calculated by using the following formula: $V = [\text{length} \times (\text{width})^2]/2$. After measuring the tumor volume, the treated mice were sacrificed by using the CO_2 inhalation method, and the major vital organs like lung, liver, kidney, heart, and brain were collected and then immediately fixed in 10% paraformaldehyde in PBS solution for the histopathological study. The vital organs were embedded in paraffin and sliced into 4 μm sections using a microtome and then placed onto the slide and stained with H&E (hematoxylin and eosin) and observed using a Nikon light microscope.

Statistical Analysis. The data were calculated as the mean ± standard deviation (SD) of the experiments performed in triplicates. Statistical comparisons were carried out using student's *t*-test. $^*p \leq 0.05$ was considered to be significant.

■ ASSOCIATED CONTENT

Supporting Information

The Supporting Information is available free of charge on the ACS Publications website at DOI: 10.1021/acsomega.7b01347.

Stability data of the formulated FA-PEG@BBR-AgNP nanomaterial in 10% mouse serum (mSerum) and 0.01 M concentration of PBS (PDF)

■ AUTHOR INFORMATION

Corresponding Author

*E-mail: skperiyaruniv@gmail.com.

ORCID

Ramasamy Bhanumathi: 0000-0002-5494-079X

Notes

The authors declare no competing financial interest.

■ ACKNOWLEDGMENTS

This research work was supported by UGC-MRP, (grant number F.No-43-581/2014(SR)) Govt. of India. S.K./R.B. acknowledges and thankful to the EM facility center, All India Institute of Medical Sciences (AIIMS), New Delhi for EM analysis.

■ REFERENCES

(1) Ferlay, J.; Soerjomataram, I.; Dikshit, R.; Eser, S.; Mathers, C.; Rebelo, M.; Parkin, D. M.; Forman, D.; Bray, F. Cancer incidence and mortality worldwide: Sources, methods and major patterns in GLOBOCAN 2012. *Int. J. Cancer* **2015**, *136*, E359−E386.

(2) Siegel, R. L.; Miller, K. D.; Jemal, A. Cancer statistics, 2017. *Ca-Cancer J. Clin.* **2017**, *67*, 7−30.

(3) DeSantis, C. E.; Fedewa, S. A.; Sauer, A. G.; Kramer, J. L.; Smith, R. A.; Jemal, A. Breast cancer statistics, 2015: convergence of incidence rates between black and white women. *Ca-Cancer J. Clin.* **2016**, *66*, 31−42.

(4) Harris, A. L. Hypoxia—a key regulatory factor in tumor growth. *Nat. Rev. Cancer* **2002**, *2*, 38−47.

(5) Joyce, J. A.; Pollard, J. W. Micro environmental regulation of metastasis. *Nat. Rev. Cancer* **2008**, *9*, 239−252.

(6) Quail, D. F.; Joyce, J. A. Microenvironmental regulation of tumor progression and metastasis. *Nat. Med.* **2013**, *19*, 1423−1437.

(7) Asati, V.; Mahapatra, D. K.; Bharti, S. K. PI3K/Akt/mTOR and Ras/Raf/MEK/ERK signaling pathways inhibitors as anticancer agents: Structural and pharmacological perspectives. *Eur. J. Med. Chem.* **2016**, *109*, 314−341.

(8) Pappalardo, F.; Russo, G.; Candido, S.; Pennisi, M.; Cavalieri, S.; Motta, S.; McCubrey, J. A.; Nicoletti, F.; Libra, M. Computational Modeling of PI3K/AKT and MAPK Signaling Pathways in Melanoma Cancer. *PLoS One* **2016**, *11*, e0152104.

(9) Kondoh, M.; Ohga, N.; Akiyama, K. Hypoxia-induced reactive oxygen species cause chromosomal abnormalities in endothelial cells in the tumor microenvironment. *PLoS One* **2013**, *8*, e80349.

(10) Anderson, E. J.; Neufer, P. D. Type II skeletal myofibers possess unique properties that potentiate mitochondrial H_2O_2 production. *Am. J. Physiol.: Cell Physiol.* **2005**, *290*, C844−C851.

(11) Kuo, H. P.; Chuang, T. C.; Yeh, M. H.; Hsu, S. C.; Way, T. D.; Chen, P. Y.; Wang, S. S.; Chang, Y. H.; Kao, M. C.; Liu, J. Y. Growth suppression of HER2-overexpressing breast cancer cells by berberine via modulation of the HER2/PI3K/Akt signaling pathway. *J. Agric. Food Chem.* **2011**, *59*, 8216−8224.

(12) Lin, C. C.; Yang, J. S.; Chen, J. T.; Fan, S.; Yu, F. S.; Yang, J. L.; Lu, C. C.; Kao, M. C.; Huang, A. C.; Lu, H. F.; Chung, J. G. Berberine induces apoptosis in human HSC-3 oral cancer cells *via* simultaneous activation of the death receptor-mediated and mitochondrial pathway. *Anticancer Res.* **2007**, *27*, 3371−3378.

DOI: 10.1021/acsomega.7b01347
ACS Omega 2018, 3, 8317−8328

(13) Mantena, S. K.; Sharma, S. D.; Katiyar, S. K. Berberine inhibits growth, induces G1 arrest and apoptosis in human epidermoid carcinoma A431 cells by regulating Cdki-Cdk-cyclin cascade, disruption of mitochondrial membrane potential and cleavage of caspase 3 and PARP. *Carcinogenesis* **2006**, *27*, 2018−2027.
(14) Kim, S.; Han, J.; Lee, S. K.; Choi, M.-Y.; Kim, J.; Lee, J.; Jung, S. P.; Kim, J. S.; Kim, J. H.; Choe, J.-H.; Lee, J. E.; Nam, S. J. Berberine Suppresses the TPA-Induced MMP-1 and MMP-9 Expressions Through the Inhibition of PKC-alpha in Breast Cancer Cells. *J. Surg. Res.* **2012**, *176*, e21−e29.
(15) Fu, L.; Chen, W.; Guo, W.; Wang, J.; Tian, Y.; Shi, D.; Zhang, X.; Qiu, H.; Xiao, X.; Kang, T.; Huang, W.; Wang, S.; Deng, W. Berberine Targets AP-2/hTERT, NF-κB/COX-2, HIF-1α/VEGF and Cytochrome-c/Caspase Signaling to Suppress Human Cancer Cell Growth. *PLoS One* **2013**, *8*, e69240.
(16) Rawat, D. S.; Thakur, B. K.; Semalty, M.; Semalty, A.; Badoni, P.; Rawat, M. S. M. Baicalein-phospholipid complex: a novel drug delivery technology for phytotherapeutics. *Curr. Drug Discovery Technol.* **2013**, *10*, 224−232.
(17) Oh, Y. J.; Choi, G.; Choy, Y. B.; Park, J. W.; Park, J. H.; Lee, H. J. Aripiprazole-montmorillonite: a new organic-inorganic nanohybrid material for biomedical applications. *Chem.—Eur. J.* **2013**, *19*, 4869−4875.
(18) Jeong, J. K.; Gurunathan, S.; Kang, M. H.; Han, J. W.; Das, J.; Choi, Y. J.; Kwon, D. N.; Cho, S. G.; Park, C.; Seo, H. G.; Song, H.; Kim, J. H. Hypoxia-mediated autophagic flux inhibits silver nanoparticle triggered apoptosis in human lung cancer cells. *Sci. Rep.* **2016**, *6*, 1−13.
(19) Ditto, A. J.; Shah, K. N.; Robishaw, N. K.; Panzner, M. J.; Youngs, W. J.; Yun, Y. H. The Interactions between L-Tyrosine Based Nanoparticles Decorated with Folic Acid and Cervical Cancer Cells under Physiological Flow. *Mol. Pharmaceutics* **2012**, *9*, 3089−3098.
(20) Cheng, W.; Nie, J.; Xu, L.; Liang, C.; Peng, Y.; Liu, G.; Wang, T.; Mei, L.; Huang, L.; Zeng, X. pH-Sensitive Delivery Vehicle Based on Folic Acid-Conjugated Polydopamine-Modified Mesoporous Silica Nanoparticles for Targeted Cancer Therapy. *ACS Appl. Mater. Interfaces* **2017**, *9*, 18462−18473.
(21) Dong, P. V.; Ha, C. H.; Binh, L. T.; Kasbohm, J. Chemical synthesis and antibacterial activity of novel-shaped silver nanoparticles. *Int. Nano Lett.* **2012**, *2*, 9.
(22) Liu, F.; Deng, D.; Chen, X.; Qian, Z.; Achilefu, S.; Gu, Y. Folate-Polyethylene Glycol Conjugated Near-Infrared Fluorescence Probe with High Targeting Affinity and Sensitivity for *In Vivo* Early Tumor Diagnosis. *Mol. Imaging Biol.* **2010**, *12*, 595−607.
(23) Murugan, C.; Rayappan, K.; Thangam, R.; Bhanumathi, R.; Shanthi, K.; Vivek, R.; Thirumurugan, R.; Bhattacharyya, A.; Sivasubramanian, S.; Gunasekaran, P.; Kannan, S. Combinatorial nanocarrier based drug delivery approach for amalgamation of anti-tumor agents in breast cancer cells: an improved nanomedicine strategy. *Sci. Rep.* **2016**, *6*, 1−17.
(24) Chen, S. K.; Hsu, C. H.; Tsai, M. L.; Chen, R. H.; Drummen, G. Inhibition of Oxidative Stress by Low-Molecular-Weight Polysaccharides with Various Functional Groups in Skin Fibroblasts. *Int. J. Mol. Sci.* **2013**, *14*, 19399−19415.
(25) Benyettou, F.; Rezgui, R.; Ravaux, F.; Jaber, T.; Blumer, K.; Jouiad, M.; Motte, L.; Olsen, J. C.; Platas-Iglesias, C.; Magzoub, M.; Trabolsi, A. Synthesis of Silver Nanoparticles for the Dual Delivery of Doxorubicin and Alendronate to Cancer Cells. *J. Mater. Chem. B* **2015**, *3*, 7237−7245.
(26) Raut, R. W.; Lakkakula, J. R.; Kolekar, N. S.; Mendhulkar, V. D.; Kashid, S. B. Phytosynthesis of Silver Nanoparticle Using *Gliricidia sepium* (Jacq.). *Curr. Nanosci.* **2009**, *5*, 117−122.
(27) Dai, X.; Song, H.; Liu, W.; Yao, S.; Wang, G. On-line UV-NIR spectroscopy as a process analytical technology (PAT) tool for on-line and real-time monitoring of the extraction process of Coptis Rhizome. *RSC Adv.* **2016**, *6*, 10078−10085.
(28) Sharma, A.; Tapadia, K. Silver Nanoparticles-Based Nano-drop Spectrophotometric Determination of Cationic Surfactants Coupled with Hydrophobic Interaction; An Application to Pharmaceuticals and Environmental Samples. *Orient. J. Chem.* **2016**, *32*, 2641−2651.
(29) Lam, P. L.; Lee, K. K. H.; Kok, S. H. L.; Cheng, G. Y. M.; Tao, X. M.; Hau, D. K. P.; Yuen, M. C. W.; Lam, K. H.; Gambari, R.; Chui, C. H.; Wong, R. S. M. Development of formaldehyde-free agar/gelatin microcapsules containing berberine HCl and gallic acid and their topical and oral applications. *Soft Matter* **2012**, *8*, 5027−5037.
(30) Chandrasekar, D.; Sistla, R.; Ahmad, F. J.; Khar, R. K.; Diwan, P. V. Folate coupled poly (ethylene glycol) conjugates of anionic poly (amidoamine) dendrimer for inflammatory tissue-specific drug delivery. *J. Biomed. Mater. Res., Part A* **2007**, *82*, 92−103.
(31) Xue, M.; Yang, M.-X.; Zhang, W.; Li, X. M.; Gao, D. H.; Ou, Z. M.; Li, Z. P.; Liu, S. H.; Li, X. J.; Yang, S. Y. Characterization, pharmacokinetics, and hypoglycemic effect of berberine loaded solid lipid nanoparticles. *Int. J. Nanomed.* **2013**, *8*, 4677−4687.
(32) Vimala, K.; Shanthi, K.; Sundarraj, S.; Kannan, S. Synergistic effect of chemo-photothermal for breast cancer therapy using folic acid (FA) modified zinc oxide nanosheet. *J. Colloid Interface Sci.* **2017**, *488*, 92−108.
(33) Agnihotri, S.; Mukherji, S.; Mukherji, S. Size-controlled silver nanoparticles synthesized over the range 5−100 nm using the same protocol and their antibacterial efficacy. *RSC Adv.* **2014**, *4*, 3974−3983.
(34) Chen, J.; Huang, L.; Lai, H.; Lu, C.; Fang, M.; Zhang, Q.; Luo, X. Methotrexate-Loaded PEGylated Chitosan Nanoparticles: Synthesis, Characterization, and in Vitro and in Vivo Antitumoral Activity. *Mol. Pharmaceutics* **2014**, *11*, 2213−2223.
(35) Saad, M.; Garbuzenko, O. B.; Minko, T. Co-delivery of siRNA and an anticancer drug for treatment of multidrug-resistant cancer. *Nanomedicine* **2008**, *3*, 761−776.
(36) Bhanumathi, R.; Vimala, K.; Shanthi, K.; Thangaraj, R.; Kannan, S. Bioformulation of Silver Nanoparticles as Berberine Carrier cum Anticancer Agent against Breast Cancer. *New J. Chem.* **2017**, *41*, 14466−14477.
(37) Murugan, C.; Venkatesan, S.; Kannan, S. Cancer Therapeutic Proficiency of Dual-Targeted Mesoporous Silica Nanocomposite Endorses Combination Drug Delivery. *ACS Omega* **2017**, *2*, 7959−7975.
(38) Liu, L.; Liu, J.; Wang, Y.; Yan, X.; Sun, D. D. Facile synthesis of monodispersed silver nanoparticles on graphene oxide sheets with enhanced antibacterial activity. *New J. Chem.* **2011**, *35*, 1418−1423.
(39) Akhavan, O.; Ghaderi, E.; Aghayee, S.; Fereydooni, Y.; Talebi, A. The use of glucose-reduced graphene oxide suspension for photothermal cancer therapy. *J. Mater. Chem.* **2012**, *22*, 13773−13781.
(40) Vivek, R.; Thangam, R.; NipunBabu, V.; Rejeeth, C.; Sivasubramanian, S.; Gunasekaran, P.; Muthuchelian, K.; Kannan, S. Multifunctional HER2-Antibody Conjugated Polymeric Nanocarrier Based Drug Delivery System for Multi-Drug-Resistant Breast Cancer Therapy. *ACS Appl. Mater. Interfaces* **2014**, *6*, 6469−6480.
(41) Rayappan, K.; Murugan, C.; Sundarraj, S.; Lara, R. P.; Kannan, S. Peptide-Conjugated Nano-Drug Delivery System to Improve Synergistic Molecular Chemotherapy for Colon Carcinoma. *Chem. Select* **2017**, *2*, 8524−8534.
(42) Liu, F.; Deng, D.; Chen, X.; Qian, Z.; Achilefu, S.; Gu, Y. Folate-polyethylene glycol conjugated near-infrared fluorescence probe with high targeting affinity and sensitivity for *in vivo* early tumor diagnosis. *Mol. Imaging Biol.* **2010**, *12*, 595−607.
(43) Panyam, J.; Zhou, W. Z.; Prabha, S.; Sahoo, S. K.; Labhasetwar, V. Rapid endo-lysosomal escape of poly(DL-lactide-co-glycolide) nanoparticles: implications for drug and gene delivery. *FASEB J.* **2002**, *16*, 1217−1226.

DOI: 10.1021/acsomega.7b01347
ACS Omega 2018, 3, 8317−8328